



Article

# Quantum Interference and Nonequilibrium Josephson Currents in Molecular Andreev Interferometers

Noel L. Plaszkó <sup>1,†</sup>, Peter Rakyta <sup>1,†</sup> , József Cserti <sup>1</sup> , Andor Kormányos <sup>1,\*,†</sup> and Colin J. Lambert <sup>2,\*</sup>

<sup>1</sup> Department of Physics of Complex Systems, Eötvös Loránd University, Budapest 1095, Pázmány P. s. 1/A, Hungary; plaszkonoel@gmail.com (N.L.P.); rakytap@caesar.elte.hu (P.R.); cserti@elte.hu (J.C.)

<sup>2</sup> Department of Physics, Lancaster University, Lancaster LA1 4YB, UK

\* Correspondence: andor.kormanyos@complex.elte.hu (A.K.); c.lambert@lancaster.ac.uk (C.J.L.)

† These authors contributed equally to this work.

Received: 21 April 2020; Accepted: 21 May 2020; Published: 28 May 2020



**Abstract:** We study the quantum interference (QI) effects in three-terminal Andreev interferometers based on polyaromatic hydrocarbons (PAHs) under non-equilibrium conditions. The Andreev interferometer consists of a PAH coupled to two superconducting and one normal conducting terminals. We calculate the current measured in the normal lead as well as the current between the superconducting terminals under non-equilibrium conditions. We show that both the QI arising in the PAH cores and the bias voltage applied to a normal contact have a fundamental effect on the charge distribution associated with the Andreev Bound States (ABSs). QI can lead to a peculiar dependence of the normal current on the superconducting phase difference that was not observed in earlier studies of mesoscopic Andreev interferometers. We explain our results by an induced asymmetry in the spatial distribution of the electron- and hole-like quasiparticles. The non-equilibrium charge occupation induced in the central PAH core can result in a  $\pi$  transition in the current-phase relation of the supercurrent for large enough applied bias voltage on the normal lead. The asymmetry in the spatial distribution of the electron- and hole-like quasiparticles might be used to split Cooper pairs and hence to produce entangled electrons in four terminal setups.

**Keywords:** superconductivity; molecular electronics; quantum interference; Cooper pair splitting

## 1. Introduction

Quantum interference (QI) is ubiquitous in nature. Constructive quantum interference (CQI) leads to the formation of energy levels in atoms or molecules and energy bands in crystals, whereas destructive quantum interference (DQI) leads to energy gaps in molecules and band gaps in solids. The energy scale for these QI phenomena can be up to a few  $eV$  and therefore these quantum effects control the properties of molecules and solids at room temperature, for which  $k_B T \approx 25 \text{ meV} \ll 1 \text{ eV}$ . In addition to these high temperature manifestations of QI, many low-temperature interference phenomena are well known, such as superfluidity and superconductivity, which occur on energy scale of order a few  $meV$  or less.

Investigations of QI in condensed systems are often driven by the desire to harness QI and deliver useful function. For example, when a molecule is placed into the nanogap between two metallic electrodes, it is known that electron transport from the source to the drain electrode is phase coherent at room temperature, provided the length of the molecule is less than approximately 3 nm. Consequently, if the interference pattern created by electronic de Broglie waves passing through the molecule can be controlled, then useful room-temperature devices such as molecular-scale

switches, transistors and sensors could be realised. Single-molecule electronics is the sub-field of nanoelectronics [1–7], which aims to deliver such structures and in pursuing this goal, many groups have demonstrated that electrons can be injected into (and collected from) the core of a molecule with atomic accuracy [8–11]. Furthermore, it has been demonstrated that an ability to vary the atomic-scale connectivity to molecular cores is an effective way of controlling room-temperature QI [12,13]. On the other hand, at lower temperatures, quantum engineers strive to utilise QI in superconducting structures such as superconductor quantum interference devices (SQUIDs) and Andreev interferometers, which rely on controlling the interplay between a superconducting condensate and charge-carrying quasi-particles [14–22]. In such devices, QI is controlled by the phase of the superconducting order parameter, which describes a macroscopic collective degree of freedom, which has no counterpart at room temperature.

In this article, we examine the interplay between the high-energy-scale QI found in molecules and the low-temperature QI present in superconductors. Our aim is to determine how an ability to control the connectivity to molecular cores with atomic accuracy can be used to engineer the properties of Andreev interferometers and SQUIDs.

From the viewpoint of connectivity, a fundamental manifestation of QI is illustrated in Figure 1 top and middle panels, which shows an anthanthrene molecular core (consisting of 6 six-membered rings) connected by triple bonds to external electrodes. The connectivity of the triple bonds to the core is fixed by chemical synthesis. Figure 1 shows two examples of molecules with different connectivities. Following the numbering scheme of the lattice shown at the bottom of Figure 1, molecule 1 has triple bonds connected to atoms 12 and 3, whereas molecule 2 has triple bonds connected to atoms 9 and 22. The triple bonds are connected to terminal aryl rings, which in turn are connected to thioacetate anchor groups, which bind the molecules to source and drain electrodes. Since the triple bonds form weak links to the central core, it is conceptually convenient to consider the combination of an aryl ring, anchor group and external electrode as a single “compound electrode”, (coloured blue in Figure 1) which injects or collects electrons to or from the central core, via the triple bonds. Remarkably, when the external electrodes are normal (i.e., not superconducting), the room-temperature electrical conductance of setup 1 is both measured and predicted [23] to be approximately 81 times larger than that of setup 2. As explained in Reference [23], this conductance ratio is a clear manifestation of room-temperature QI. From the viewpoint of superconductivity, our aim is to replace one or more of the normal electrodes by superconducting electrodes and examine how electron transport through such molecular cores is controlled by a combination of connectivity and by the phase of the superconducting order parameter.

In ballistic normal-superconductor (*N-S*) hybrid systems the fundamental transport process is Andreev reflection, whereby an incoming electron is reflected back as a hole at the *N-S* interface. A rich set of physical phenomena that follow from this scattering process was realized in Andreev interferometers, which are devices with two (or more) superconducting and one (or more) normal leads attached to a central region [14,15]. For example, due to the extraordinary sensitivity of the Andreev current to the superconducting phase difference, Andreev interferometers may provide a faster and more precise alternative to superconductor quantum interference devices (SQUIDs) [16] to measure properties of quantum systems or even detecting Majorana bound states [17]. Importantly, the presence of a normal lead allows one to change the equilibrium occupation of Andreev bound states formed in multi-terminal *N-S* systems. It was suggested that such a non-equilibrium effect can be used to engineer  $\pi$ -Josephson junctions [18,19], where the fundamental relation  $I_s = I_c \sin(\delta\Phi)$  between the phase difference  $\delta\Phi$  of the order parameters of two superconductors and the supercurrent  $I_s$  can be changed to  $I_s = I_c \sin(\delta\Phi + \pi)$  ( $I_c$  is the critical current). This effect has indeed been measured in diffusive meso-scopic multi-terminal *N-S* systems [20–22].

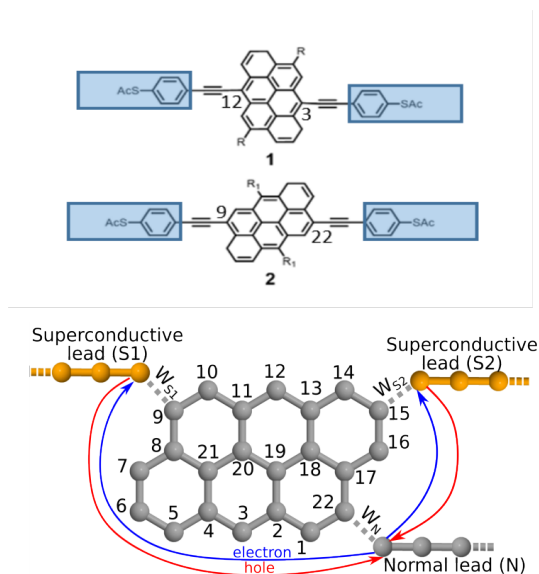


**Figure 1.** The top and middle panels show molecules 1 and 2, with connectivities 12,3 and 9,22 to the anthanthrene molecular core. The lower panel shows an Andreev interferometer consisting of an anthanthrene molecule, two superconducting leads and one normal lead. The “sites” of the associated tight-binding model represent  $p_z$  orbitals of the anthanthrene molecule and are labelled according to the figure. The coupling of the molecule to the normal (superconducting) lead is denoted by  $W_N$  ( $W_S$ ), for details see the text. The superconducting leads are characterized by a superconducting order parameter  $\Delta e^{i\phi_1}$  and  $\Delta e^{i\phi_2}$ . The transport processes responsible for the conventional interference effect are indicated by solid lines for the electron-like (blue) and hole-like (red) propagation.

Recently, the superconducting properties of molecular-scale junctions have also started to attract experimental [24–27] as well as theoretical [28–30] interest. In Reference [30] we discussed the equilibrium properties of various multiterminal  $N$ - $S$  systems where, in particular, QI effects in the core of the molecule play an important role. Here we show how such QI effects and non-equilibrium charge injection can lead to interesting effects in molecular Andreev interferometers. Namely, the non-equilibrium occupation of the Andreev bound states (ABSs) which are formed in superconductor-molecule-superconductor ( $S$ - $M$ - $S'$ ) Josephson junctions can be driven via the third, normal lead attached to the Josephson junction, thus realizing a non-equilibrium  $N$ - $M$ - $SS'$  system. As already mentioned, one of the key ingredients in our work is QI which arises in the molecular core of  $N$ - $M$ - $SS'$  systems that are based on polyaromatic hydrocarbons (PAHs) [12,13,23]. We find that in these systems one may observe effects that were not attainable in previously studied mesoscopic Andreev interferometers. Based on the “magic number theory of connectivity in References [12,23,30] we show that conductive channels through the molecular core can give rise to interfering paths contributing to the total ABS wave function with the same or with an opposite sign for electron and hole-like degrees of freedom. This rich set of interfering paths is provided by the conductive channels opened by the insertion of a substituent heteroatom into the molecular core [13]. Under specific circumstances the interplay of the interfering amplitudes may even lead to the total suppression of the electron-like (or hole-like) degrees of freedom on certain molecular sites and, at the same time, to a constructive interference for the hole-like (or electron-like) charge carriers. Since the charge current through the normal lead is closely tied to the Andreev reflection process, its magnitude is highly influenced by the density of both the electron- and hole-like particles in the vicinity of the normal contact. Thus, by measuring the charge current through the normal lead one can also probe the electron-hole separation in the molecular junction.

In what follows, we first describe the main characteristics of interference effects in Andreev interferometers based on PAHs [12,13,23] in equilibrium conditions. Our choice is justified by the peculiar mid-gap transport properties of these molecules accompanied by inner quantum interference

effects within the core of the molecule [12,13,30–42]. We outline an illustrative connectivity-based theory that can be used to understand the current-phase relations at non-equilibrium conditions as well. Then we present our numerical results obtained for the normal and for the supercurrent at finite bias applied on the normal lead. We interpret our results in terms of connectivity arguments. We examine how the electrical properties of the Andreev interferometers would be influenced by tuning the inner QI effects of the molecular core. We demonstrate how QI can lead to a suppression of the normal current which is a clear evidence of the spatial separation of the electron- and hole-like particles. Finally, we present a summary of our most important results and give a brief outlook.

## 2. Results

From a conceptual viewpoint the key ingredients of our theoretical model are based on weak coupling, connectivity-driven, mid-gap transport and phase coherence. A detailed explanation of these assumptions is given in References [12,23,30]. Here we only mention that the term “weak coupling” means that the central aromatic molecule is weakly coupled to the contacts resulting in a small level broadening and self energy correction to the highest occupied molecular orbital (HOMO) and lowest unoccupied molecular orbital (LUMO) levels compared to the HOMO-LUMO gap. Thus, provided the Fermi level lies within the gap (resulting in near mid-gap transport), the quantum interference effects in the phase coherent transport processes are characterized by the properties of the molecular core alone. (The Coulomb interactions can be included at the level of a self-consistent mean field description such as Hartree, or Hartree-Fock.) Taken together, these conditions ensure that when computing the Green’s function of the core, the contribution of the electrodes can be ignored. Consequently, the probability of the propagation of the charged particles between sites  $k$  and  $l$  of the molecule is described by the “magic number” matrix element [12,23,30]  $M_{kl} \sim g_{kl}$ , where  $g(E_F) = (E_F - H_{\text{mol}})^{-1}$  is the Green’s function of the isolated molecule described by Hamiltonian  $H_{\text{mol}}$ . In particular, the electrical conductance corresponding to connectivity  $k, l$  is proportional to  $|M_{kl}|^2$ . In the simplest theoretical description an integer valued connectivity matrix  $H_{\text{mol}}$  captures the complexity of the inner CQI and DQI effects within the core of the molecule and when  $E_F$  coincides with the middle of the HOMO-LUMO gap, the resulting magic number matrix  $M_{kl}$  is simply a table of integers. In particular, for the bipartite lattice of Figure 1, when  $E_F$  coincides with the middle of the HOMO-LUMO gap, destructive quantum interference arises between sites  $k$  and  $l$  that have the same parity (i.e., both are odd or both are even) and therefore the matrix element  $M_{kl}$  is zero. In contrast, when the sites  $k$  and  $l$  have different parity,  $M_{kl}$  may be finite giving a non-zero propagation amplitude of the charged particles between sites  $k$  and  $l$ . For the anthanthrene core of Figure 1,  $M_{3,12} = 9$  and  $M_{9,22} = 1$ . Hence their conductance ratio is predicted to be  $|M_{3,12}|^2/|M_{9,22}|^2 = 81$ , which is close to the measured value of the conductance ratio, both for single molecules and for self-assembled monolayers [12,23,43].

### 2.1. Theoretical Background: Equilibrium Molecular Andreev Interferometers

In order to understand the unconventional non-equilibrium Andreev interference effect described in the next sections, following Reference [30] we first give a brief overview of the considerations that explain the interference pattern in the current  $I_N$  flowing through the normal lead as a function of the superconducting phase difference  $\delta\Phi = \phi_1 - \phi_2$  between the S1 and S2 leads (see Figure 1) in equilibrium. Under equilibrium conditions, the limit  $eV \rightarrow 0$  is understood, where  $V$  is the applied bias on lead  $N$  with respect to the chemical potential of the superconductors. Note that the imposition of a phase difference  $\delta\Phi$  also generates a Josephson current  $I_s$  flowing between the superconducting leads. Experimentally, as shown in References [44,45],  $\delta\Phi$  can be controlled, thus allowing the measurement of the current-phase relation (CPR) of the supercurrent  $I_s$  and the phase dependence of  $I_N$ .

Let us investigate  $I_N$  in a device consisting of an anthanthrene central molecular core, as shown in Figure 1. The  $\delta\Phi$  dependence of  $I_N$  can be understood as a result of an interference effect between the possible transport paths of electrons and holes.

The arms of the interferometer are formed by the trajectories  $N \rightarrow \text{mol} \rightarrow S1 \rightarrow \text{mol} \rightarrow N$  and  $N \rightarrow \text{mol} \rightarrow S2 \rightarrow \text{mol} \rightarrow N$ . Let us consider the setup in which the normal lead  $N$  is attached to site labeled by 22, and the superconducting leads  $S1$  and  $S2$  are attached to sites 9 and 15, respectively and examine the transmission amplitude  $t_{9,22}$  related to the process  $N \rightarrow \text{mol} \rightarrow S1 \rightarrow \text{mol} \rightarrow N$ . Since the normal reflection on the superconductors does not give a contribution to the charge current, only Andreev reflection [46] can cause a net charge current. During Andreev reflection, an incoming electron-like quasiparticle is converted into a hole-like quasiparticle and vice versa at the normal-superconductor interface. Due to the Andreev reflection, an extra  $e^{-i\phi_1}$  phase factor multiplies the transmission amplitude ( $\phi_1$  is the phase of the superconductor  $S1$ ). Then, the reflected hole-like state propagates back to the normal lead, a process which can be described by  $-M_{9,22}$  according to the Bogoliubov-de Gennes equation [30]. Based on these considerations, the transmission amplitude can be written in the following form

$$t_{9,22} \sim -M_{9,22}^2 e^{-i\phi_1}. \quad (1)$$

Similar considerations can be made for the transmission amplitude  $t_{15,22}$ . Since there are two interfering arms in the interferometer, one needs to sum up both transmission amplitudes associated with the two propagation paths to calculate the total transmission amplitude:

$$t_{tot} \sim t_{9,22} + t_{15,22} = -M_{9,22}^2 e^{-i\phi_1} - M_{15,22}^2 e^{-i\phi_2}, \quad (2)$$

From this expression the Andreev current  $I_N$  at small bias voltage ( $eV \ll \Delta$ ) can be approximated as:

$$I_N \sim |t_{tot}|^2 = M_{9,22}^4 + M_{15,22}^4 + 2 \cdot M_{9,22}^2 \cdot M_{15,22}^2 \cdot \cos(\phi_1 - \phi_2). \quad (3)$$

As one can see, the Andreev current  $I_N$  is indeed expected to show a simple dependence on the superconducting phase difference  $\delta\Phi = \phi_1 - \phi_2$  with a minimum at  $\pi$ . Regarding the supercurrent  $I_s$  flowing between  $S1$  and  $S2$ , in first approximation, this can be understood as a consequence of Andreev bound states (ABS), although a continuum of unbound states can also add a finite contribution [47].

## 2.2. Non-Equilibrium Numerical Calculations

To avoid time-dependent order parameter phases varying at the Josephson frequency, we assume that the superconductors  $S1$  and  $S2$  share a common condensate chemical potential  $\mu$ . A finite bias voltage  $V$  (with respect to  $\mu$ ) can be then applied to the normal lead. This bias voltage will affect both the normal current  $I_N$  and, by changing the equilibrium occupation of the ABSs, the supercurrent  $I_s$  as well.

In order to describe the transport properties at finite bias voltage one has to use a theoretical framework capable of describing non-equilibrium transport processes. We calculate the currents  $I_N$  and  $I_s = (I_{S_1} - I_{S_2})/2$  by using a tight binding approach and the Keldysh non-equilibrium Green's function techniques [48–50]:

$$I_{N(S_i)} = -\frac{2e}{h} \text{Re} \left[ \int dE \text{Tr} \left( \tau_3 \Gamma_{N(S_i)} G^<(E) \right) \right], \quad (4)$$

with  $\Gamma_{N(S_i)}$  being the coupling from the molecule to the normal (superconducting) lead labeled by  $N$  ( $S_i$ ) including the electron-hole degrees of freedom and  $\tau_3$  is the third Pauli matrix acting on the electron-hole space. The current  $I_{N(S_i)}$  describes the current flowing through lead  $N$  ( $S_i$ ) into the central molecule. In the steady state limit the currents flowing through the individual leads satisfy the charge conservation rule  $I_N + I_{S_1} + I_{S_2} = 0$  leading to two independent currents  $I_N$  and  $I_s$  characterizing the electrical properties of the junction. Finally, the lesser Green's function  $G^<$  in Equation (4) can be calculated within the Keldysh non-equilibrium framework using the Keldysh equation (see details in the Appendix B). The calculations were performed using the tight-binding framework implemented

in the EQuUs [51] package. The relevant electronic states in the molecular core were described by a single orbital tight-binding model where the nearest neighbor sites are connected by a hopping amplitude  $\gamma_0$ . As shown in Figure 1, the hopping amplitude between the molecule and the normal  $N$  (superconducting  $S1, S2$ ) lead is given by  $W_N$  ( $W_{S1}, W_{S2}$ ). In our calculations, unless indicated otherwise, we used  $W_N = 0.1\gamma_0$  and  $W_S = 0.3\gamma_0$ . The normal and superconducting contacts were modeled by a one-dimensional tight-binding chain. The magnitude of the superconducting order parameter in the leads  $S1$  and  $S2$  was  $\Delta = 3 \times 10^{-3}\gamma_0$ . The results that we are going to discuss do not depend on the actual value of  $\gamma_0$  and  $\Delta$ . This simple model is justified by previous studies of connectivity driven transport processes through PAH molecules [12,23,30]. Following these works, our aim is to highlight the role of connectivity in the transport properties of these molecular cores leading to new interference phenomena. We give the remaining details of the tight binding-model used in our calculations in Appendix A.

### 2.3. Non-Equilibrium Molecular Andreev Interferometers

As a first example of non-equilibrium effects in Andreev-interferometers it is instructive to consider the system shown in Figure 2. With respect to Figure 1, we changed the connecting sites of the leads in order to “disarm” one of the interfering arms. This can be achieved by choosing connecting sites such that the magic number matrix elements between the sites connected to the normal lead and to one of the superconducting leads becomes zero, as shown in Figure 2. Therefore one may expect  $I_N$  to be independent of the superconducting phase. Note, however, that the magic number  $M_{6,9}$  between the superconducting leads is finite. Therefore, as we will show later, an ABS is formed in this system and it has an important effect on  $I_N$ . The results for  $\delta\Phi$  and  $eV$  dependence of  $I_N$  can be seen in Figure 3a. The current  $I_N$  remains very small for applied voltages  $eV \ll \Delta$  on the normal lead. As  $eV$  is increased, a finite  $I_N$  starts to flow, but in contrast to the  $\sim \cos \delta\Phi$  dependence given in Equation (3),  $I_N$  exhibits a *maximum* at superconducting phase difference  $\delta\Phi = \pi$ .

These results can be explained by the effect of an ABS. As pointed out in earlier studies on multiterminal normal-superconductor mesoscopic systems [18,19], the voltage  $eV$  sets the effective electrochemical potential for the ABSs and those with energy  $E_{n,ABS}(\delta\Phi) \leq eV$  are filled. The ABS energy  $E_{n,ABS}(\delta\Phi)$  depends on the phase difference  $\delta\Phi$ . A change in the occupation of the ABSs directly affects  $I_{S1}$  and  $I_{S2}$  and therefore the current distribution in the Andreev-interferometer junction will depend on both the voltage  $eV$  and on the phase difference  $\delta\Phi$ . To illustrate these effects we show the supercurrent  $I_s = (I_{S1} - I_{S2})/2$  in Figure 3b. As  $eV$  is increased, a deviation from the simple  $I_s = I_c \sin(\delta\Phi)$  relation can be clearly seen and for  $eV > \Delta$  a  $\pi$ -transition takes place in  $I_s$ , similarly to what was obtained in References [18,19].

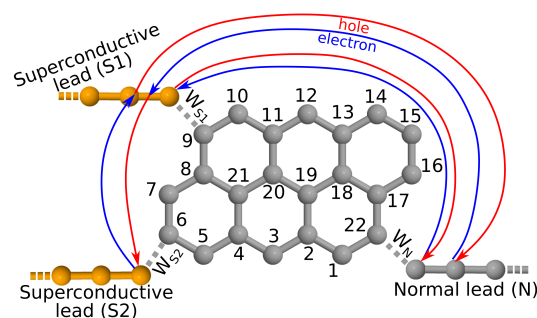


**Figure 2.** Anthanthrene molecule attached to two superconducting and one normal lead. The connectivity matrix element between the sites 6 and 22 is zero, while the connectivity between sites 9 and 22 and between sites 9 and 6 is finite. Solid lines indicate the propagation of the electron-like (blue) and hole-like (red) quasiparticles.

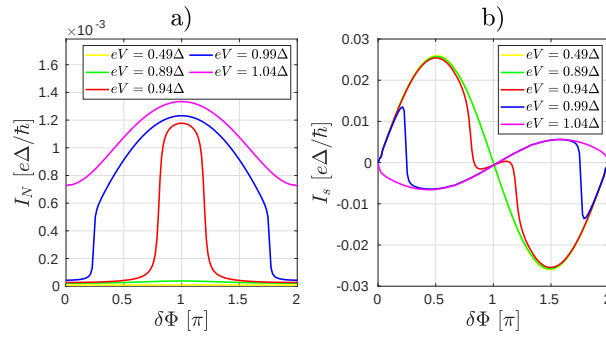


**Figure 3.** The currents  $I_N$  (a) and  $I_s$  (b) as a function of the phase difference  $\delta\Phi$  between the superconducting leads for the system depicted in Figure 2 for several bias voltage  $eV$ . (a) a robust peak in  $I_N$  appears around the phase the difference  $\pi$  when the bias voltage is comparable to the superconducting gap  $\Delta$ . (b) the supercurrent shows a  $\pi$  transition for  $eV > \Delta$ .

One can give a heuristic argument of why the presence of ABSs can affect  $I_N$ . This argument draws on analogies with the discussion given for the equilibrium case, that is, it is based on interfering quasiparticle trajectories. Although in the system depicted in Figure 2 the connectivity between the normal lead and the superconducting lead S2 is zero, the charge carriers can still probe the phase of lead S2 when they propagate along a path that also includes an Andreev reflection from the lead S1. Namely, as illustrated in Figure 2, both  $M_{22,9}$  and  $M_{6,9}$  are finite. We denote the amplitude of such propagation by  $t_{6,22}^{(9)}$ , where the upper index (9) indicates that the propagation between the sites 6 and 22 takes place via site the 9. To approximate the amplitude  $t_{6,22}^{(9)}$  one can make similar considerations as in the previous section. Thus,

$$t_{6,22}^{(9)} \sim (-M_{22,9}) \cdot e^{-i\phi_1} \cdot M_{9,6} \cdot e^{i\phi_2} \cdot (-M_{6,9}) \cdot e^{-i\phi_1} \cdot M_{9,22}. \quad (5)$$

This amplitude describes a (a) propagation from the normal lead to the superconducting electrode S1 ( $M_{9,22}$ ), (b) Andreev reflection from electrode S1 ( $e^{-i\phi_1}$ ), (c) propagation of the hole-like state from contact S1 to S2 ( $-M_{6,9}$ ), (d) Andreev reflection of the hole-like particle on the contact S2 ( $e^{i\phi_2}$ ), (e) electron-like propagation between the superconducting electrodes S1 and S2 ( $M_{9,6}$ ), (f) a third Andreev reflection on the superconducting electrode S1 ( $e^{-i\phi_1}$ ), (g) and a hole-like propagation from the contact S1 to the normal lead ( $-M_{22,9}$ ). Finally, we also take into account in our minimal model the amplitude  $t_{9,22}$  describing the direct propagation between the normal lead and the lead S1 according to Equation (1). The observed interference effect can be explained as the interplay between these two amplitudes:

$$I_N \sim |t_{9,22} + t_{6,22}^{(9)}|^2 = M_{9,22}^4 \cdot \left(1 + M_{9,6}^4 - 2 \cdot M_{9,6}^2 \cdot \cos(\phi_1 - \phi_2)\right). \quad (6)$$

The normal current  $I_N$  in Equation (6) has a maximum at phase difference  $\phi_1 - \phi_2 = \pi$ . The minus sign appearing in front of the  $\cos(\phi_1 - \phi_2)$  term in Equation (6) is due to the peculiar properties of the Bogoliubov-de Gennes quasiparticles. Namely, the amplitude  $t_{6,22}^{(9)}$  contains one more hole-like propagation compared to the amplitude  $t_{9,22}$ , which brings in an extra minus sign needed for the formation of the unconventional interference effect. Note, that this argument does not explain why the increase in  $I_N$  appears only above a certain bias voltage. Moreover, the transport process associated to the amplitude  $t_{6,22}^{(9)}$  contains four more tunnelings between the superconducting leads and the molecular core compared to the amplitude  $t_{9,22}$ . Thus, the amplitude  $t_{9,22}$  might be expected to be much larger than the amplitude  $t_{6,22}^{(9)}$  which would suppress the interference effect between these two interfering paths.

The role of the ABSs can be shown explicitly by using Green's function theory to calculate the differential conductance  $\frac{dI_N}{dV}$ . The details of this calculation are presented in the Appendix B.

For simplicity, let us assume that there is only one ABS in the system. (The general case of more than one ABS is also discussed in the Appendix B). Then the differential conductance can be approximated as [52]

$$\frac{dI_N}{deV} \approx \frac{16e}{h} \frac{\Gamma_{ABS}^e \Gamma_{ABS}^h}{(eV - E_{ABS})^2 + \Gamma_{ABS}^2}, \quad (7)$$

where  $\Gamma_{ABS} = \Gamma_{ABS}^e + \Gamma_{ABS}^h$  is the level broadening of the ABS due to the presence of the normal lead,  $\Gamma_{ABS}^e = \langle ABS, e | W_N^\dagger \text{Im}(g_N^e) W_N | ABS, e \rangle$  with  $W_N$  being the coupling between the normal lead and the central molecule,  $W_N^\dagger$  is the Hermitian conjugate of  $W_N$ ,  $g_N^e$  stands for the electron-like block of the surface Green's function of the normal contact evaluated at energy  $E_{ABS}$ ,  $\text{Im}(\dots)$  denotes the imaginary part of a function, and  $|ABS, e\rangle$  represents the electron-like components of the wave function of the ABS. The definition of  $\Gamma_{ABS}^h$  is analogous to  $\Gamma_{ABS}^e$  involving the hole-like degrees of freedom instead of the electron-like components. According to Equation (7), the ABS leads to a resonant peak of Lorentzian lineshape in the differential conductance for  $eV \approx E_{ABS}(\delta\Phi)$ . The half-width of the resonance is determined by the finite lifetime of the ABS which is due to the coupling to the normal lead given by  $\Gamma_{ABS}^e$  and  $\Gamma_{ABS}^h$ . We note that a similar result can be obtained for a system hosting multiple ABSs. The total differential conductance in this case would be a sum of resonances centered on the energies of the individual ABSs'. However, the "cross-talk" between the ABSs has an additional influence on the shape of the resonances, that is, they start to deviate from the regular Lorentzian shape. (For details see the Appendix B.)

Looking back to Equation (6), one may now say that the interfering amplitude  $t_{6,22}^{(9)}$  can be increased due to the Fabry-Perot-like resonant oscillations of the charged particles between the superconducting contacts. These oscillations lead to the formation of ABSs of finite lifetime, which, in turn, affect the current  $I_N$  at finite  $eV$ , as indicated by Equation (7).

The ABSs can be visualized by calculating the density of states of the junction (see Appendix C for details). The results of such calculations for the system in Figure 2 are shown in Figure 4. In Figure 4a,b we show the density of states for two different coupling  $W_N$ . The large values of the density of states (bright region) indicate the ABS. In this particular case, for  $eV = 0$  and zero temperature there is only one occupied ABS (at energy  $-E$ , not shown) and one unoccupied ABS [at energy  $E$ , Figure 4a,b]. By applying a finite  $eV > 0$  the occupation of these ABSs can be changed, leading to the peculiar dependence of both  $I_N$  and  $I_s$  on  $\delta\Phi$  in Figure 3 that we noted earlier. Because of the normal lead, the ABSs have a finite lifetime, which is determined by the escape rate of the particles through the normal lead. Therefore, the ABS lifetime (and consequently the width of the resonant peaks in the differential conductance) is expected to be sensitive to the coupling between the normal lead and the central molecule. This can be clearly seen in Figure 4c,d, where the peak of the differential conductance calculated for  $W_N = 0.1\gamma_0$  is considerably narrower than the peak calculated for  $W_N = 0.3\gamma_0$ . Notice, that for higher values of  $W_N$  the resonant peak starts to deviate from the Lorentzian shape. This is because by increasing the coupling between the contacts and the central molecule one can no longer neglect the energy dependence of the Green's function of the normal contact in the calculation of  $\Gamma_{ABS}^e$  and  $\Gamma_{ABS}^h$ , see Appendix B for details. Since the ABSs energy  $E_{ABS}$  depends on the phase difference  $\delta\Phi$ , the peaks in  $\frac{dI_N}{deV}$  are also sensitive to the superconducting phase difference. This is also shown in Figure 4c,d. Therefore, by measuring  $\frac{dI_N}{deV}$  as a function of  $\delta\Phi$  one may obtain spectroscopic information about the ABSs [18].

The role of ABSs and QI in the molecular core can be further illustrated by studying the finite bias properties of the system shown already in Figure 1, bottom panel. For this configuration of the leads the magic number vanishes between the two sites where the superconducting electrodes are attached. One may therefore expect that there is no ABS present in the system. According to our calculations this is not exactly the case: one can find an ABS whose energy is very close to the value of the pair potential  $\Delta$  in the leads, but it is nearly independent of  $\delta\Phi$  and therefore it can carry only a small supercurrent. This explains that for a finite bias  $eV$  the  $\delta\Phi$  dependence of  $I_N$  remains qualitatively the same as in

the zero bias case discussed in Equation (1)–(3) and shows a minimum at  $\delta\Phi = \pi$  for all bias voltages (Figure 5a).

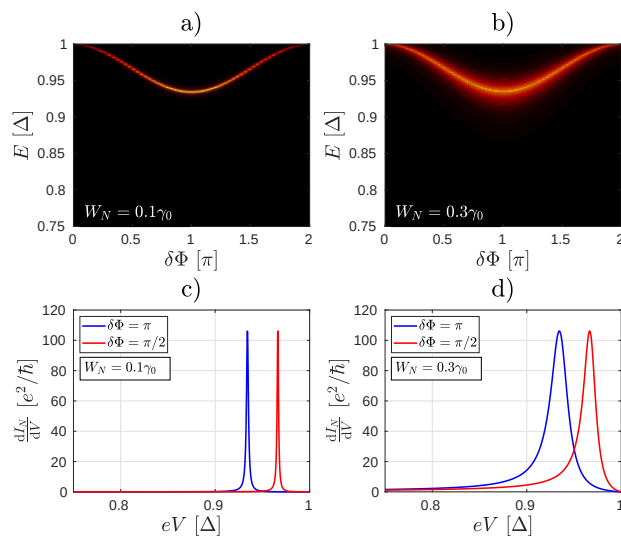


**Figure 4.** (a,b) Density of states of the molecular junction shown in Figure 2 for two different coupling  $W_N$  of the normal lead to the molecule. The bright areas indicate the dispersion of the Andreev Bound State (ABS) as a function of  $\delta\Phi$ . The ABS energy level is broadened by increasing  $W_N$ . (c) A resonance occurs in the differential conductance when the bias voltage  $eV$  is close to the energy  $E_n(\delta\Phi)$  of the ABS in (a). (d) As the ABS is broadened, the width of the resonance broadens as well.

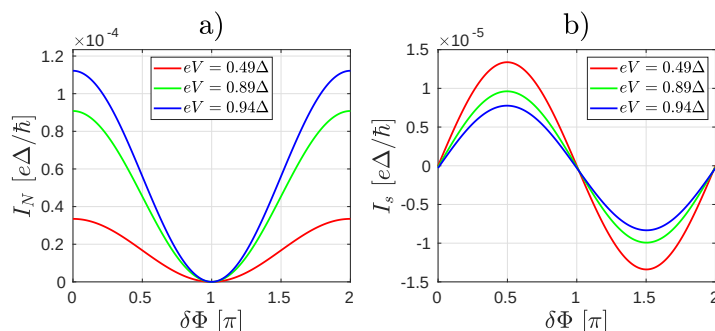


**Figure 5.** The currents  $I_N$  (a) and  $I_s$  (b) as a function of the phase difference  $\delta\Phi$  between the superconducting leads for the system depicted in Figure 1 for several bias voltage  $eV$ . (a) the Andreev current  $I_N$  shows a minimum at  $\delta\Phi = \pi$ . (b) The current-phase dependence of supercurrent is  $I_s \propto \sin \delta\Phi$ .

The supercurrent  $I_s$  shows the conventional  $\propto \sin \delta\Phi$  dependence for  $eV < \Delta$  [Figure 5b]. By comparing Figure 5a,b, one can see that although a small  $I_s$  can flow for finite  $eV$ , the critical current  $I_c$  is smaller than  $I_N$ . This is the opposite of what we found in the previous case [Figure 3]. Overall, one may also notice that both  $I_N$  and  $I_c$  are much smaller than previously, c.f. Figures 3 and 5.

These results underpin the importance of ABSs in Andreev interferometers and are also a consequence of mid-gap transport. Namely, the propagation amplitude described by the Green's function elements decay with the energy difference between the chemical potential and the energy of the eigenstates. Since the energy levels of the molecule are much further from the chemical potential than the ABS levels, their contribution to the Green's function elements will be also much smaller than the contribution of the ABSs. Thus, in the mid-gap energy regime, the transport processes would indeed be dominated by the interference effects related to the ABSs.

We now discuss the most general situation, where ABSs can be found in the system and, in contrast with the case in Figure 1, the connectivity from the normal lead to both superconducting terminal is

finite. In what follows we shall examine the unconventional interference effects as the connectivity in the interferometer is changed. We consider a setup similar to the one shown in Figure 1 and tune the asymmetry of the molecular interferometer by inserting a substitutional heteroatom into the molecular core [13], that is, a carbon atom is replaced by a substituent heteroatom, as indicated schematically in Figure 6a. Due to the presence of the heteroatom, new conductive channels open up in the molecular core that were originally closed via destructive QI effects. In our theoretical model we account for the presence of a substitutional heteroatom by a modified on-site energy on a specific site in the molecule. By changing for example, the on-site energy  $\varepsilon_3$  in the tight-binding Hamiltonian of the molecular core [see Figure 6a], the normal conductance between sites labeled by even numbers also becomes finite [13]. Assuming that instead of S1 and S2 we have normal conducting leads N1 and N2 as in Figure 6a, the evolution of the ratio of the zero-bias normal conductances  $\sigma_{N,N1}$  and  $\sigma_{N,N2}$  as a function of the on-site energy  $\varepsilon_3$  is demonstrated in Figure 6b. As one can see, by varying  $\varepsilon_3$  one can gradually open a conductive channel between leads N and N2.

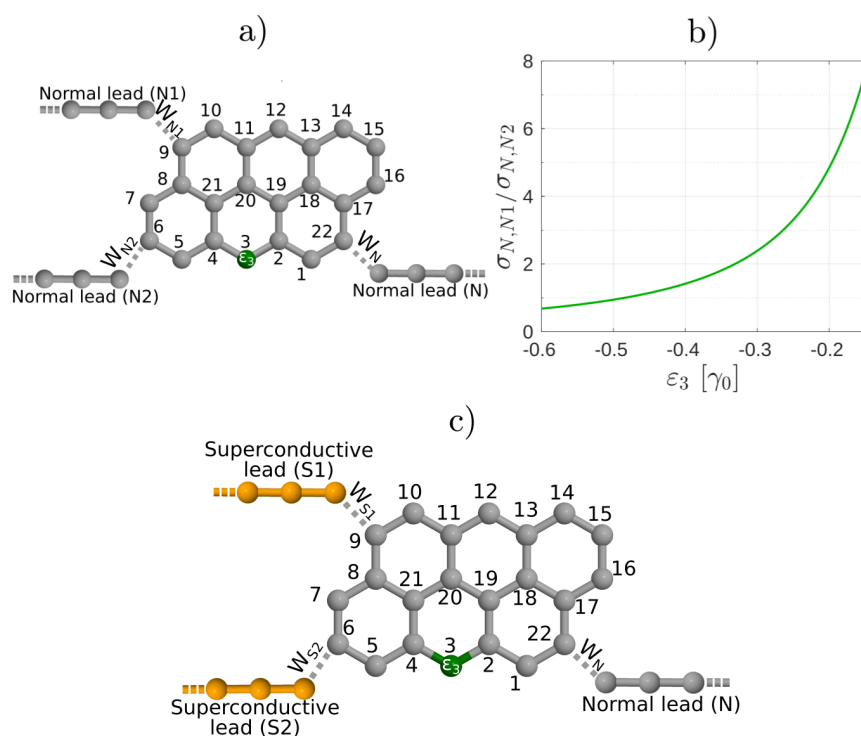


**Figure 6.** (a) Schematics of Anthranthrene molecule with a heteroatom denoted by green. (b) Ratio of the normal conductance between contacts  $N - N2$  and  $N - N1$  as a function of the on-site energy  $\varepsilon_3$  in Figure 6. At  $\varepsilon_3 = 0$  the conductance  $\sigma_{N,N1}$  between contacts  $N$  and  $N1$  is much larger than the conductance  $\sigma_{N,N2}$  between contacts  $N$  and  $N2$ , in agreement with References [12,23]. For finite  $\varepsilon_3$  the conductance  $\sigma_{N,N2}$  increases and can be comparable to  $\sigma_{N,N1}$ . (c) Andreev interferometer setup obtained by replacing the normal leads  $N1$  and  $N2$  in (a) by superconducting ones  $S1$  and  $S2$ .

We now consider the finite bias properties of the Andreev interferometer shown in Figure 6c, which can be obtained by replacing the normal leads  $N1$  and  $N2$  by superconducting ones  $S1$  and  $S2$  in Figure 6a. First, we calculate  $I_N$  for several values of  $\varepsilon_3$  and fixed  $eV = 0.95\Delta$ . Remarkably, as shown in Figure 7a,  $I_N$  takes on a hat-like shape with two maxima around the phase difference  $\pi$  for such values of  $\varepsilon_3$ , where  $\sigma_{N,N1}$  and  $\sigma_{N,N2}$  are comparable. This is clearly different from the results in Figure 3a and we are not aware of similar results in mesoscopic NS systems. Regarding  $I_s$  [Figure 7b], for smaller values of  $\varepsilon_3$  where  $\sigma_{N,N1} \gg \sigma_{N,N2}$ , it is qualitatively similar to the results shown in Figure 3b. On the other hand, the current-phase relation of  $I_s$  becomes similar to the conventional  $I_s = I_c \sin \delta\Phi$  as the conductive channel gradually opens between  $N$  and  $S2$  and consequently  $\sigma_{N,N1} \approx \sigma_{N,N2}$

[see for example, the case  $\varepsilon_3 = -0.50\gamma_0$  in Figure 7b]. Note that in this case the  $I_s(\delta\Phi)$  dependence for  $\delta\Phi \approx \pi$  is different from the corresponding  $eV = 0.94\Delta$  result shown in Figure 3b.

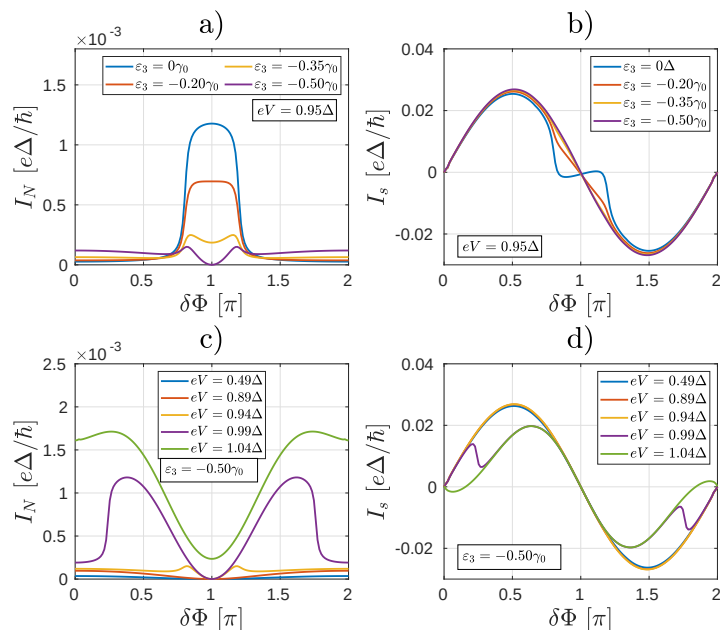


**Figure 7.** The currents (a)  $I_N$  and (b)  $I_s$  (b) as a function of the phase difference  $\delta\Phi$  between the superconducting leads for the system depicted in Figure 6a for several values of the on-site energy  $\varepsilon_3$  and fixed bias  $eV = 0.95\Delta$ .  $I_N$  starts to show a double peak structure as a function of  $\delta\Phi$  for  $\varepsilon_3 \approx -0.20\gamma_0$ . (c)  $I_N$  and (d)  $I_s$  as a function of the bias voltage  $eV$  for  $\varepsilon_3 = -0.50\gamma_0$ .

In Figure 7c,d we show  $I_N$  and  $I_s$ , respectively, as a function of  $\delta\Phi$  for several biases  $eV$ . Here we fixed  $\varepsilon_3 = -0.50\gamma_0$ , that is,  $\sigma_{N,N1} \approx \sigma_{N,N2}$ . As one can see, for small  $eV$ , when the occupation of the ABS is not yet modified,  $I_N$  shows qualitatively the same behavior as in Figure 5a, that is, when there was no current-carrying ABS in the system. For larger  $eV$ , however, there is a clear difference with respect to both Figures 3a and 5a, since  $I_N$  adopts a hat-like dependence on  $\delta\Phi$ . The non-equilibrium population of the ABSs also affects  $I_s$  [see Figure 7d] which starts to deviate from the  $\propto \sin \delta\Phi$  dependence for  $eV > 0.95\Delta$ .

According to our calculations the presence of a heteroatom does not modify the ABS spectrum significantly [Figure 8a]. As shown in Figure 8b, when  $I_N$  nearly vanishes for  $\varepsilon_3 = -0.50\gamma_0$ ,  $\delta\Phi = \pi$  [Figure 7a], the differential conductance  $\frac{dI_N}{deV}$  vanishes, too. According to Equation (7), the vanishing of  $\frac{dI_N}{deV}$  can be explained only if the coupling between the normal lead and the ABS vanishes.

Therefore we turn our attention to the electron- and hole-like broadening terms  $\Gamma_n^e$  and  $\Gamma_n^h$  in the numerator of Equation (7). In Figure 8c,d we show the local density of states (LDOS) on the molecular site connected to the normal contact separately for the electron- and hole-like degrees of freedom. Note that  $\Gamma_n^e$  and  $\Gamma_n^h$  are proportional to the corresponding LDOS. As one can see, the electron-like component of the LDOS becomes highly suppressed at phase difference  $\delta\Phi = \pi$ , while the hole-like components has a maximum there. In turn, we found that on other sites of the molecule the hole-like component of the LDOS can be suppressed and the electron-like LDOS enhanced (an example is shown in Appendix D).

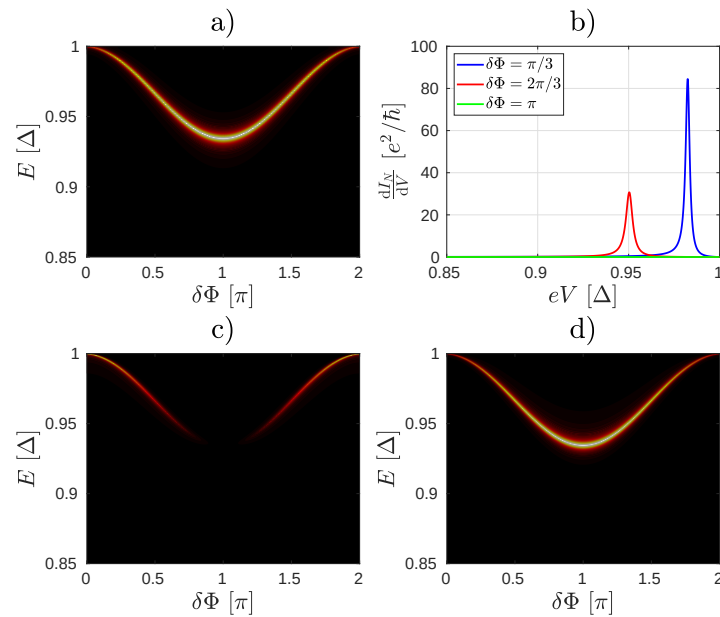


**Figure 8.** (a) The density of states of the ABS for the case shown in Figure 6c. (b) The differential conductance corresponding to (a). The local density of states for electron (c) and hole (d) quasiparticles as a function of  $\delta\Phi$ . In these calculations we used  $\varepsilon_3 = -0.50\gamma_0$ .

The surprising result in Figure 8c,d can be understood as a peculiar interference effect that acts in a different way on the electron- and the hole-like particles. (Note, that due to electron-hole symmetry, the same feature can be observed for negative energies with a constructive interference in the electron-like part of the LDOS and with a destructive interference in the hole-like part of the LDOS.) One can give the following simple argument in terms of new quasiparticle paths. In Figure 9 we show two quasiparticle trajectories. The first trajectory, shown in Figure 9a, describes the process  $N \rightarrow S2 \rightarrow S1 \rightarrow N$  and the last segment  $S1 \rightarrow N$  is made possible by the fact that the substitutional heteroatom opened a new conductive channel. Using a similar argument as in the case of Equation (5), one can argue that the amplitude of the path contributing to the electron-like part of the wave function can be expressed as

$$\begin{aligned} t_{\text{odd}}^e &\sim M_{N,S1} \cdot e^{i\phi_1} \cdot (-M_{S1,S2}) \cdot e^{-i\phi_2} \cdot M_{S2,N} \\ &\sim -M_{N,S1} \cdot M_{S1,S2} \cdot M_{S2,N} e^{i(\phi_1 - \phi_2)}. \end{aligned} \quad (8)$$

Since  $t_{\text{odd}}^e$  contains an odd number of propagations through the molecule, and the sign of the propagation depends on whether one considers electron- or hole-like particles, the amplitude  $t_{\text{odd}}^h$  contributing to the hole-like component of the wave function would differ by a minus sign compared to  $t_{\text{odd}}^e$ . Now consider the process  $N \rightarrow S2 \rightarrow S1 \rightarrow S2 \Rightarrow N$  depicted in Figure 9b. The last propagation indicated by  $S2 \Rightarrow N$  describes a normal reflection (without electron-hole conversion) at the site connected to  $S2$  and a forthcoming propagation to the normal contact. (Since we are working in the weak coupling limit, the normal reflection at sites connected to the contacts has a finite probability.) The amplitude corresponding to this path can be expressed as follows:

$$\begin{aligned} t_{\text{even}}^e &\sim M_{N,S2} \cdot M_{S2,S1} \cdot e^{i\phi_1} \cdot (-M_{S1,S2}) \cdot e^{-i\phi_2} \cdot M_{S2,N} \\ &\sim -M_{N,S2}^2 \cdot M_{S1,S2}^2 \cdot e^{i(\phi_1 - \phi_2)}. \end{aligned} \quad (9)$$

Since  $t_{\text{even}}^e$  depends on the square of the connectivity matrix elements, the corresponding hole-like amplitude  $t_{\text{even}}^h$  would have the same sign as  $t_{\text{even}}^e$ . One can see that because of the sign difference, there is a destructive interference in total amplitude  $t^e = t_{\text{even}}^e + t_{\text{odd}}^e$  and a constructive one in  $t^h = t_{\text{even}}^h + t_{\text{odd}}^h$ . This example shows how differences can appear in the processes that determine

the electron-like and the hole-like LDOS. Note that, strictly speaking, in the calculation of  $t^e$  and  $t^h$  one would need to take into account all possible scattering paths and not only those discussed above. We expect, however, that the described interference effect would not be affected significantly.

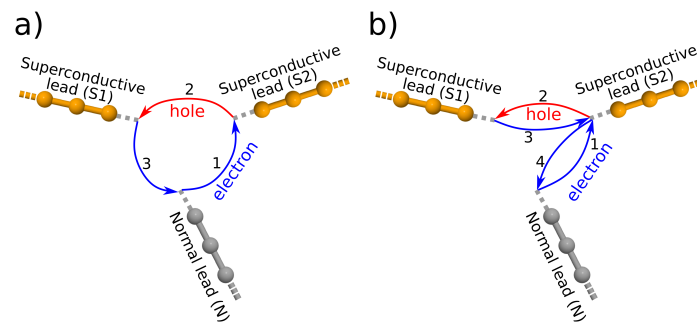


**Figure 9.** (a) An example for interfering paths having an amplitude of opposite sign for the electron- and hole-like particles. These kinds of paths have an odd number of propagation through the molecular core. (b) A representative of trajectories consisting of even number of propagations through the molecular core. The amplitude of these kinds of trajectories have the same sign for the electron- and hole-like quasiparticles.

We also mention that according to our numerical results the interference effect can be swapped between the electron- and hole-like components by changing the sign of the on-site energy  $\varepsilon_3$  of the heteroatom. According Equation (8) of Reference [13] the connectivity matrix element  $M_{N,S1}$  can change a sign for sufficiently large heteroatom on-site energy. Consequently,  $t_{odd}^e$  would also change sign resulting in a constructive interference for the electron-like and destructive interference for the hole-like components in the LDOS.

Opening of new conductance channels can affect the properties of the molecular Andreev interferometer not only in the case discussed in Figures 6 and 7, where the conductance between the leads  $N$  and  $S1$  was tuned. As noted earlier for the system in Figure 1, for this configuration of the leads the connectivity matrix element is zero between the two sites where the superconducting electrodes are attached. However, this connectivity matrix element can also be made finite by adding a heteroatom as indicated in Figure 10a. This means changing the onsite energy  $\varepsilon_{12}$  in the tight-binding Hamiltonian of the molecular core. We found that the dependence of the supercurrent on  $\varepsilon_{12}$  and  $eV$  is qualitatively similar to the behavior in Figure 7b,c. Therefore we only show the calculations for  $I_N$  in Figure 10b. As the connectivity grows for larger values of  $\varepsilon_{12}$ , the  $\delta\Phi$  dependence of  $I_N$  also undergoes a drastic change and, interestingly, adopts a qualitatively similar behavior to the one shown in Figure 7a, that is, there are two maxima in the current around  $\delta\Phi = \pi$ .

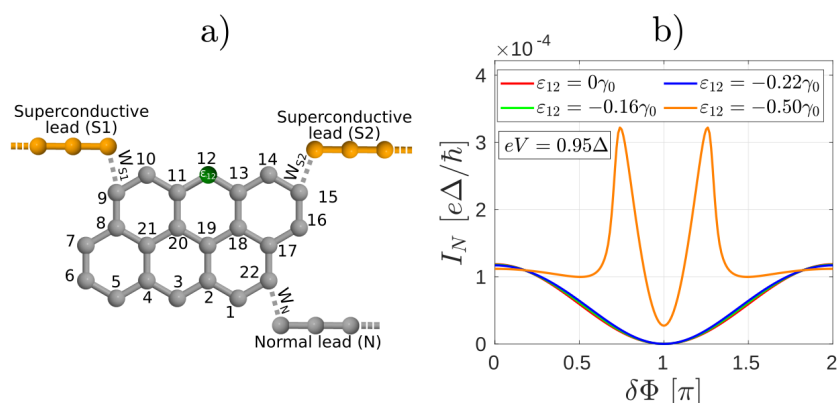


**Figure 10.** (a) Anthanthrene molecule with a heteroatom (denoted by green) and the same configuration of leads as in Figure 1. (b) The normal current  $I_N$  as a function of the phase difference  $\delta\Phi$  between the superconducting leads for the setup in (a).

### 3. Conclusions

In this article, we have investigated the interplay between two quantum interference phenomena that take place on hugely different energy scales; QI within molecules, which takes place on the scale of electron volts and QI associated with superconductivity, which takes place on the scale of milli-electron volts. We studied the interplay between connectivity-driven QI in molecular cores and non-equilibrium charge distribution in three-terminal Andreev interferometers based on PAH molecules. We showed that QI determines certain fundamental properties of the ABS in the system, while their energies can be tuned by the phase difference between the superconducting probes. Consequently, QI and the non-equilibrium ABS occupation in the molecular core, which can be modified by a bias voltage applied to the normal lead, affects both the normal current and the supercurrent in the system. We gave a simplified explanation of some of the complicated interference effects in terms of electron and hole trajectories and point out when such explanation breaks down under non-equilibrium conditions. We found that the dependence of the normal current on the superconducting phase difference can exhibit a double-peak structure, while the supercurrent can show a  $\pi$  transition when the bias  $eV$  on the normal lead is larger than the superconducting gap. We also showed that adding a heteroatom to the PAH core can significantly change the QI and can induce an asymmetry in the spatial distribution of the electron- and hole-like particles, which has a direct impact on the phase dependence of the normal current. This indicates that the properties of molecular Andreev interferometers can be tuned by engineering QI in the molecular core.

For the future one may envisage a system similar to the one shown in Figure 6 but with two normal leads ( $N1$  and  $N2$ ) attached to different sites of the molecular core. Assume now that lead  $N1$  would be coupled to a site where, for example, the electron LDOS is enhanced and the hole suppressed, whereas lead  $N2$  to a site where the opposite is true, that is, the electron LDOS is suppressed and the hole LDOS is enhanced. Then the so-called non-local Andreev reflection ( $N1 \rightarrow N2$ ), where an incoming electron from lead  $N1$  is Andreev reflected into lead  $N2$ , would be enhanced with respect to local Andreev reflection ( $N1 \rightarrow N1$ ) and normal electron transmission ( $N1 \rightarrow N2$ ). Therefore, in such four-terminal device the asymmetry between the electron- and hole-like degrees of freedom on certain sites of the molecular core could be translated into a spatial separation of electron pairs originating from the superconducting condensate. This process is called Cooper pair splitting and it provides entangled electron pairs that may play an important role in quantum information processing. Most of the proposed Cooper pair splitters to-date relied on Coulomb blockade transport through quantum dots [53–56], or on peculiar properties of novel low-dimensional materials [57–59]. Our results indicate that Cooper pair splitting may also be achieved in multi-terminal molecular systems where the spatial separation of the Cooper pairs would rely on the inner QI effects of the molecule. The detailed study

of such four-terminal molecular Cooper pair splitters is an interesting problem which we leave to a future work.

**Author Contributions:** The concept of the manuscript was developed by P.R., A.K. and C.J.L. The computational methodology and the EQuUs software was developed by P.R. and N.L.P. The project was supervised by P.R., J.C. and A.K. The first draft of the manuscript was written by P.R., A.K. and C.J.L. Funding for the project was acquired by C.J.L. and J.C. All authors have read and agreed to the published version of the manuscript.

**Funding:** N.L.P., P.R., A.K. and J.C. were supported by NKFIH within the Quantum Technology National Excellence Program (Project No. 2017-1.2.1-NKP-2017-00001) and this work was completed in the ELTE Institutional Excellence Program (1783-3/2018/FEKUTSRAT) supported by the Hungarian Ministry of Human Capacities. P.R. and A.K. was also supported by Hungarian Scientific Research Fund, OTKA Grant No. NN 127903 (Topograph FlagERA project). P.R. acknowledges the funding from OTKA PD123927 and K123894, and N.L.P. was supported by the ÚNKP-19-1 New National Excellence Program of the Ministry for Innovation and Technology. C.J.L. acknowledges financial support from the UK EPSRC, through grant nos. EP/M014452/1, EP/P027156/1 and EP/N03337X/1. This work was additionally supported by the European Commission is provided by the FET Open project 767187—QUIET.

**Conflicts of Interest:** The authors declare no conflict of interest.

## Abbreviations

The following abbreviations are used in this manuscript:

ABS	Andreev Bound States
CQI	Constructive Quantum interference
DQI	Destructive Quantum interference
LDOS	Local density of states
PAH	polyaromatic hydrocarbons
QI	Quantum interference
SQUID	Superconducting quantum interference device

## Appendix A. The Tight-Binding Model of the Molecular Junctions

To describe the electrical transport processes in the studied molecular junctions we use a nearest neighbor tight binding model catching the dynamics of the  $p_z$  electrons of the molecular core.

The tight binding parameters describing the molecular core are chosen following the philosophy in References [12,23], where the aim is to highlight the role of connectivity in determining the transport properties of these molecular cores. For this reason, the hopping integrals  $\gamma_{ii'} = \gamma_0$  are set to unity and the on-site energies  $\varepsilon_i$  are set to zero, see Figure A1. In other words, the unit of energy is the hopping integral and the site energy is the energy origin. This means that the Hamiltonian of the molecule is simply a connectivity matrix and therefore all predicted effects are results of the connectivity alone. Remarkably, as demonstrated in References [12,23], this approach yields the experimentally-measured conductance ratios of a range of PAHs. The normal and superconducting contacts are modeled by a one-dimensional tight-binding chain. The transport properties of the junction have a weak dependence on the actual physical parameters of the leads as far as the leads remains metallic in the studied energy regime. Thus, we chose the physical parameters of the leads to increase the density of states in the leads and have the bandwidth of the conductive channel larger than the studied energy regime. In particular, we set the hopping amplitude in the contacts to  $0.05\gamma_0$  and the on-site energy parameter to 0. The superconducting contacts are modeled by an s-type superconducting pair potential  $\Delta = 3 \times 10^{-3}\gamma_0$  and the pair potential is zero everywhere else in the system.

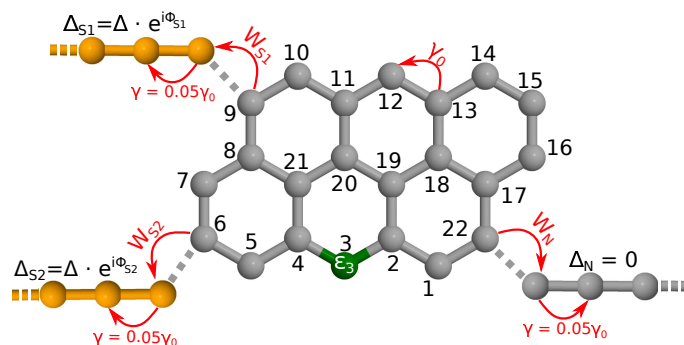


**Figure A1.** The tight binding model of the Anthanthrene molecule attached to two superconductive and one normal lead. The sites in the molecular core represent  $p_z$  orbitals of the anthanthrene molecule and are labelled according to the figure. The hopping amplitude between the sites of the molecular core is denoted by  $\gamma_0$ . The normal (in grey) and superconducting (in yellow) contacts are modeled by one-dimensional conductive channels. The hopping amplitude between the normal (superconducting) lead and the molecular core is given by  $W_N$  ( $W_S$ ).

As we explained in the main text, we tuned the transport properties of the molecular core by inserting a substitutional heteroatom into the molecular core. According to Reference [13], the presence of the heteroatom have a strong influence on the inner quantum interference effects in the molecular core, including the possibility that new conductive channels open up in the molecular core. In our theoretical model we account for the presence of a substitutional heteroatom by a modified on-site energy on a specific site in the molecule, see also Figure A1.

## Appendix B. Theoretical Background to Calculate the Differential Conductance

In this section we give the technical details to calculate and analyze the differential conductance on the normal lead connected to an Andreev interferometer. The aim of this section is twofold. Firstly we obtain a closed formula which can be evaluated numerically. Secondly, we answer the questions raised in the discussion of the results in Figure 3 of the main text. Namely, the reported unconventional interference effect is manifested only above a certain bias voltage applied on the normal lead. Secondly, the amplitude of the interfering path  $N \rightarrow \text{mol} \rightarrow S2 \rightarrow \text{mol} \rightarrow N$  depicted in Figure 3 of the main text is expected to be much smaller than the amplitude of the interfering path  $N \rightarrow \text{mol} \rightarrow S1 \rightarrow \text{mol} \rightarrow S2 \rightarrow \text{mol} \rightarrow N$  depicted in Figure 3 of the main text involves four extra tunnelings between the leads and the central molecule compared to the interfering path  $N \rightarrow \text{mol} \rightarrow S2 \rightarrow \text{mol} \rightarrow N$ .)

The Andreev current can be evaluated using Equation (4) of the main text. In this equation the lesser Green's function  $G^<$  can be calculated within the Keldysh non-equilibrium framework using the Keldysh equation [48–50,60,61]:

$$G^< = G^R \Sigma^< G^A, \quad (\text{A1})$$

where  $G^R(E)$  [ $G^A(E)$ ] is the retarded [advanced] Green's function and  $\Sigma^<(E) = \Sigma_{S1}^<(E) + \Sigma_{S2}^<(E) + \Sigma_N^<(E, V)$  contains the lesser self energies of the leads.

The differential conductance can be derived from Equation (4) of the main text utilizing the relation given by Equation (A1):

$$\frac{dI_N}{deV} = -\frac{2e}{h} \text{Re} \left\{ \frac{d}{deV} \int dE \text{Tr} \left[ \tau_3 W_N G^R \left( \Sigma_{S1}^< + \Sigma_{S2}^< + \Sigma_N^<(eV) \right) G^A \right] \right\} \quad (\text{A2})$$

This expression can be further simplified by applying the derivation with respect to the bias voltage  $V$  on the integrand. Notice that only the self energy of the normal lead depends on  $eV$ . Hence

$$\frac{dI_N}{deV} = -\frac{2e}{h} \text{Re} \left\{ \int dE \text{Tr} \left[ \tau_3 W_N G^R \frac{d}{deV} \Sigma_N^<(E, eV) G^A \right] \right\} \quad (\text{A3})$$

Furthermore, the lesser self energy  $\Sigma_N^<(E, eV)$  depends on the bias voltage via the thermal occupation number. In the electron-hole space the lesser self energy can be given as [48]

$$\Sigma_N^< = \begin{pmatrix} f_e(\Sigma_{N,e}^A - \Sigma_{N,e}^R) & 0 \\ 0 & f_h(\Sigma_{N,h}^A - \Sigma_{N,h}^R) \end{pmatrix} \quad (\text{A4})$$

$$= \begin{pmatrix} f_e \left( (g_{N,e}^R)^{-1} - (g_{N,e}^A)^{-1} \right) & 0 \\ 0 & f_h \left( (g_{N,h}^R)^{-1} - (g_{N,h}^A)^{-1} \right) \end{pmatrix}, \quad (\text{A5})$$

where  $f_e = f(E - eV)$  [ $f_h = f(E + eV)$ ] is the thermal occupation number for the electrons [holes] given by the Fermi-distribution function and  $\Sigma_{N,e}^R$  [ $\Sigma_{N,e}^A$ ] and  $\Sigma_{N,h}^R$  [ $\Sigma_{N,h}^A$ ] are the retarded [advanced] self energies of the electron-like and hole-like particles in the normal lead, uncoupled from the rest of the system. Similarly,  $g_{N,e}^R$  and  $g_{N,e}^A$  stand for the retarded and advanced Green's functions of the electron/hole-like particles in the normal lead. To calculate the retarded and advanced self energies and Green's functions we followed the numerical procedure described in Reference [62]. Also, we assume the uncoupled leads to be in thermal equilibrium.

For simplicity we will consider the zero temperature limit in our calculations. Consequently, the derivative of the Fermi distribution function is the Dirac delta function and the integral in Equation (A3) simplifies to

$$\begin{aligned} \frac{dI_N}{dV} = & -\frac{2e}{h} \text{Re} \left\{ \text{Tr} \left[ \tau_3 W_N G^R(eV) \begin{pmatrix} (g_{N,e}^R(eV))^{-1} - (g_{N,e}^A(eV))^{-1} & 0 \\ 0 & 0 \end{pmatrix} G^A(eV) \right] \right\} \\ & + \frac{2e}{h} \text{Re} \left\{ \text{Tr} \left[ \tau_3 W_N G^R(-eV) \begin{pmatrix} 0 & 0 \\ 0 & (g_{N,h}^R(-eV))^{-1} - (g_{N,h}^A(-eV))^{-1} \end{pmatrix} G^A(-eV) \right] \right\}. \end{aligned} \quad (\text{A6})$$

As we can see from Equation (A6), the key element to calculate the differential conductance is the retarded and advanced Green's functions  $G^R$  and  $G^A$ . Equation (A6) then can be directly used to calculate numerically the differential conductance in the studied three-terminal junctions.

To get further insight into the physics of the transport process we follow the logic of Reference [52] to evaluate these Green's functions in terms of the Dyson's equation. Let us denote the retarded Green's function of the unified system of the two superconducting contacts and the central molecular core by  $g_{\text{mol}}^R$ . Then the retarded Green's function of the whole Andreev interferometer can be evaluated in terms of the Dyson's equation:

$$G^R = \begin{pmatrix} (g_{\text{mol}}^R)^{-1} & -W_N^\dagger \\ -W_N & (g_N^R)^{-1} \end{pmatrix}^{-1}, \quad (\text{A7})$$

where

$$g_N^R = \begin{pmatrix} g_{N,e}^R & 0 \\ 0 & g_{N,h}^R \end{pmatrix} \quad (\text{A8})$$

is the Green's function of the normal lead containing both the electron and hole-like components. Equation (A7) yields for the individual components of the Green's function:

$$G^R = \begin{pmatrix} G_{\text{mol,mol}}^R & G_{\text{mol,N}}^R \\ G_{\text{N,mol}}^R & G_{\text{N,N}}^R \end{pmatrix} = \begin{pmatrix} g_{\text{mol}}^R (1 - W_N^\dagger g_N^R W_N g_{\text{mol}}^R)^{-1} & g_{\text{mol}}^R (1 - W_N^\dagger g_N^R W_N g_{\text{mol}}^R)^{-1} W_N^\dagger g_N^R \\ g_N^R (1 - W_N g_{\text{mol}}^R W_N^\dagger g_N^R)^{-1} W_N g_{\text{mol}}^R & g_N^R (1 - W_N g_{\text{mol}}^R W_N^\dagger g_N^R)^{-1} \end{pmatrix}. \quad (\text{A9})$$

Considering the rules of the matrix multiplication, and that the only non-zero elements of the lesser self energy of Equation (A5) are the block diagonal parts related to the leads, in order to evaluate the differential conductance (A6) it is enough to consider the  $G_{\text{mol,N}}^R$  block of the retarded Green's function and the  $G_{\text{N,N}}^A$  part of the advanced Green's function. According to the structure of Equation (A9) one finds:

$$G_{\text{N,N}}^R = g_N^R \sum_{n=0}^{\infty} \left( W_N g_{\text{mol}}^R W_N^\dagger g_N^R \right)^n = g_N^R + g_N^R W_N g_{\text{mol}}^R \sum_{n=0}^{\infty} \left( W_N g_{\text{mol}}^R W_N^\dagger g_N^R \right)^n W_N^\dagger g_N^R = g_N^R + g_N^R W_N g_{\text{mol}}^R \left( 1 - W_N^\dagger g_N^R W_N g_{\text{mol}}^R \right)^{-1} W_N^\dagger g_N^R = g_N^R + g_N^R W_N G_{\text{mol,mol}}^R W_N^\dagger g_N^R, \quad (\text{A10})$$

and

$$G_{\text{mol,N}}^R = G_{\text{mol,mol}}^R W_N^\dagger g_N^R. \quad (\text{A11})$$

We now return to the evaluation of the differential conductance given by Equation (A6). For simplicity we continue our calculations focusing on the first (electron-like) part of Equation (A6). (Due to the electron-hole symmetry of the Bogoliubov-de Gennes equations, the hole-like part would give the same result.) Inserting Equations (A10) and (A11) into Equation (A6) yields:

$$\frac{dI_N^e}{dV} = -\frac{2e}{h} \text{Re} \left\{ \text{Tr} \left[ \tau_3 W_N G_{\text{mol,N}}^R \left( \begin{pmatrix} (g_{\text{N,e}}^R)^{-1} & 0 \\ 0 & (g_{\text{N,e}}^A)^{-1} \end{pmatrix} G_{\text{N,N}}^A \right) \right] \right\} = -\frac{4e}{h} \text{Im} \left\{ \text{Tr} \left[ \tau_3 W_N G_{\text{mol,mol}}^R W_N^\dagger \left( \begin{pmatrix} \text{Im}(g_{\text{N,e}}^R) & 0 \\ 0 & 0 \end{pmatrix} (1 + W_N G_{\text{mol,mol}}^A W_N^\dagger g_N^A) \right) \right] \right\}. \quad (\text{A12})$$

In Equation (A12) we applied the identity  $g_{\text{N,e}}^R - g_{\text{N,e}}^A = 2i \text{Im}(g_{\text{N,e}}^R)$ . For simplicity let us suppose we have only one Andreev bound state (ABS) formed in the superconductor—molecular core—superconductor (S-mol-S) junction described by the Green's function  $g_{\text{mol}}^R$ . In the presence of the normal lead, the ABSs starts to leak out via the normal lead resulting in the broadening of the ABS energy levels. Since our main interest are the transport properties close to the mid of the HOMO-LUMO gap, in the relevant energy regime we do not expect any further bound states in  $G_{\text{mol,mol}}^R$  besides the ones corresponding to the ABSs. Thus, we might approximate  $G_{\text{mol,mol}}^R$  as:

$$G_{\text{mol,mol}}^R(E) \approx \frac{|ABS\rangle\langle ABS|}{E - E_{\text{ABS}} + i\Gamma_{\text{ABS}}}. \quad (\text{A13})$$

Here the state  $|ABS\rangle$  represents the wave function of the ABS in the molecule of energy  $E_{\text{ABS}}$ , and  $\Gamma_{\text{ABS}} = \langle ABS | W_N^\dagger \text{Im}(g_N^R) W_N | ABS \rangle$  is the level broadening originating from the escape rate of the particles through the normal lead [52]. The mathematical expression for  $\Gamma_{\text{ABS}}$  calculates the overlap between the ABS wave function and the self energy of the normal lead. Thus,  $\Gamma_{\text{ABS}}$  can be

divided into two distinct terms, one related to the escape rate of the electron-like and the second one to the escape rate of the hole-like particles. Namely,  $\Gamma_{ABS} = \Gamma_{ABS}^e + \Gamma_{ABS}^h$ , where:

$$\Gamma_{ABS}^e = \left\langle ABS \left| W_N^\dagger \begin{pmatrix} \text{Im} \left( g_{N,e}^R(E_{ABS}) \right) & 0 \\ 0 & 0 \end{pmatrix} W_N \right| ABS \right\rangle, \tag{A14}$$

and

$$\Gamma_{ABS}^h = \left\langle ABS \left| W_N^\dagger \begin{pmatrix} 0 & 0 \\ 0 & \text{Im} \left( g_{N,h}^R(E_{ABS}) \right) \end{pmatrix} W_N \right| ABS \right\rangle. \tag{A15}$$

Using the (A13) expression of  $G_{\text{mol,mol}}^R$  and the invariance of the  $\text{Tr}(\dots)$  function against the cyclic permutation of its arguments one obtains for the differential conductance:

$$\begin{aligned} \frac{dI_N^e}{dV} \approx & -\frac{4e}{h} \text{Im} \left\langle \frac{ABS \left| W_N^\dagger \begin{pmatrix} \text{Im} \left( g_{N,e}^R \right) & 0 \\ 0 & 0 \end{pmatrix} W_N \right| ABS \right\rangle}{eV - E_{ABS} + i\Gamma_{ABS}} \right. \\ & \left. - \frac{4e}{h} \text{Im} \left\{ \frac{\left\langle ABS \left| W_N^\dagger \begin{pmatrix} \text{Im} \left( g_{N,e}^R \right) & 0 \\ 0 & 0 \end{pmatrix} W_N \right| ABS \right\rangle \left\langle ABS \left| W_N^\dagger g_N^A \tau_3 W_N \right| ABS \right\rangle}{eV - E_{ABS} + i\Gamma_{ABS} \quad eV - E_{ABS} - i\Gamma_{ABS}} \right\}. \end{aligned} \tag{A16}$$

Now making use of the definition of the broadening parameters  $\Gamma_{ABS}^e$  and  $\Gamma_{ABS}^h$  we end up with the following expression for the differential conductance:

$$\frac{dI_N^e}{dV} \approx \frac{8e}{h} \frac{\Gamma_{ABS}^e \Gamma_{ABS}^h}{(eV - E_{ABS})^2 + \Gamma_{ABS}^2}. \tag{A17}$$

In the above expression we neglected the energy dependence of the Green's function of the normal lead in a  $\Gamma_{ABS}$  wide vicinity of the energy  $E_{ABS}$ . Accounting also for the hole-like part of the differential conductance (A6) gives an additional factor of two in the final result due to the electron-hole symmetry. Thus, the total differential conductance would be given by Equation (7) of the main text. In case we have more than one ABS in the junction, the first term of Equation (A16) would turn into a sum of Lorentzian resonances, while the second term evolves into a more complex mathematical expression:

$$\begin{aligned} & - \sum_{p,q} \text{Im} \left\{ \frac{\left\langle p \left| W_N^\dagger \begin{pmatrix} \text{Im} \left( g_{N,e}^R \right) & 0 \\ 0 & 0 \end{pmatrix} W_N \right| q \right\rangle \left\langle q \left| W_N^\dagger g_N^A \tau_3 W_N \right| p \right\rangle}{eV - E_p + i\Gamma_{pp} \quad eV - E_q - i\Gamma_{qq}} \right\} \\ & = \text{Im} \sum_{p,q} \frac{\Gamma_{pq,e}}{eV - E_p + i\Gamma_{pp}} \frac{\Gamma_{qp}^e - \Gamma_{qp}^h}{eV - E_q - i\Gamma_{qq}} \end{aligned} \tag{A18}$$

where  $|q\rangle$ ,  $E_q$  and  $\Gamma_q$  represents the wave function, the energy and the broadening of the  $q$ th ABS, and the quantities  $\Gamma_{qp}^e$  and  $\Gamma_{qp}^h$  are defined similarly to Equations (A14) and (A15), but the scalar product is taken between wave functions corresponding to different ABSs. Besides regular Lorentzian resonances [ $p = q$  terms of Equation (A18)] we see that the differential conductance is heavily influenced by the cross-talk of the individual ABSs. Mathematically the product of two fractions on the right hand side of Equation (A18) can be rewritten to a sum

$$\frac{\Gamma_{pq}^e}{eV - E_p + i\Gamma_{pp}} \frac{\Gamma_{qp}^e - \Gamma_{qp}^h}{eV - E_q - i\Gamma_{qq}} = \frac{\lambda}{eV - E_p + i\Gamma_{pp}} + \frac{\delta}{eV - E_q - i\Gamma_{qq}}, \quad (\text{A19})$$

where  $\lambda$  and  $\delta$  are in general complex numbers. (Individually both of them have singularity at  $eV = (\Gamma_{pp}E_q + \Gamma_{qq}E_p)/(\Gamma_{pp} + \Gamma_{qq})$ , but these singularities cancel each other in the sum of the two fractions.) Consequently, the imaginary part of these fractions would differ from the regular Lorentzian function and the total differential conductance in the presence of multiple ABSs would be the sum of asymmetric Lorentzian resonances centered to the energies of the ABSs. The asymmetry in the resonances is a signature of the cross-talk between the ABSs.

### Resonant Oscillation

As discussed in the main text, we try to explain the unconventional interference pattern by the interplay of the two paths depicted in Figure 2 of the main text. However the amplitude  $t_{9,22}$  (defined by Equation (1) of the main text) might be expected to be much larger than the amplitude  $t_{6,22}^{(9)}$  (defined by Equation (5) of the main text) which would suppress the interference effect between these two interfering paths.

The physical picture behind the small magnitude of  $t_{6,22}^{(9)}$  relative to  $t_{9,22}$  is associated to the particle transfer between the two superconducting banks. The four tunneling processes between the molecular core and the superconducting electrodes significantly decreases the magnitude of the interfering amplitude  $t_{6,22}^{(9)}$ . On the other hand, a resonant oscillation realized by the ABSs overwrites this physical picture. In this case the charge transport between the superconducting banks becomes resonantly amplified via the ABS and thus the amplitudes  $t_{6,22}^{(9)}$  and  $t_{9,22}$  becomes comparable. In summary, for energies close enough to the energy of an ABS the differential conductance shows an interference effect due to the resonant amplification of the interfering amplitude  $t_{6,22}^{(9)}$ , while for other energies the interference would be suppressed.

### Appendix C. Density of States

In this subsection we give the technical details to calculate the density of states of the three-terminal molecular junction, which can be used to physically interpret the numerical results obtained by Equation (4) of the main text and by Equation (A6). We calculate the density of states  $\rho$  from the equilibrium Green's function of the three-terminal molecular junction labeled by  $G_{\text{mol,mol}}^R$  in the calculations above. To be precise,  $G_{\text{mol,mol}}^R$  labels only that block of the whole Green's function which contains only the molecular degrees of freedom. Then the density of states can be defined as:

$$\rho(E) = -\frac{1}{\pi} \text{Tr} \left[ \text{Im} \left( G_{\text{mol,mol}}^R(E) \right) \right]. \quad (\text{A20})$$

As for the differential conductance,  $G_{\text{mol,mol}}^R$  can be calculated via the Dyson's Equation (A7) which is evaluated using the Eötvös Quantum Utilities (EQuUs) [51] software package.

### Appendix D. Comparison of the Local Density of States on Two Molecular Sites

As shown in Figure 8c,d of the the main text, which is reproduced below in Figure A2, the local density of states (LDOS) is suppressed for electron-like quasiparticles and enhanced for hole-like quasiparticles on molecular site 22 (for the numbering of the molecular sites, see Figure A1). We have calculated the LDOS for the other sites of the molecular core as well and found that due to QI the LDOS of the electron and hole quasiparticles is different on each site. In particular, it can happen that, in contrast to Figure A2, the electron LDOS is larger than the hole LDOS. An example shown in Figure A3, where this asymmetry of LDOS can be clearly seen.

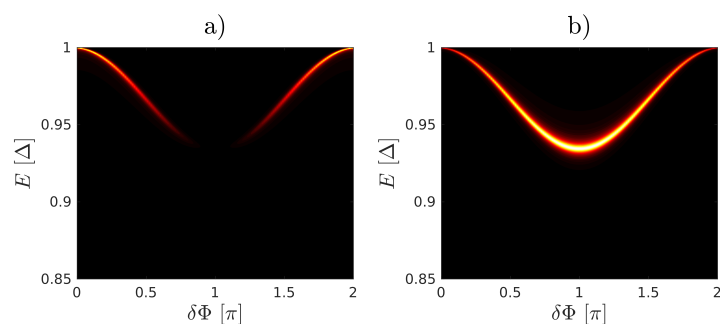


**Figure A2.** The LDOS for electron (a) and hole (b) quasiparticles as a function of  $\delta\Phi$  on molecular site 22 of the Andreev interferometer shown in Figure 6c of the main text and in Figure A1. In these calculations  $\varepsilon_3 = -0.50\gamma_0$ .

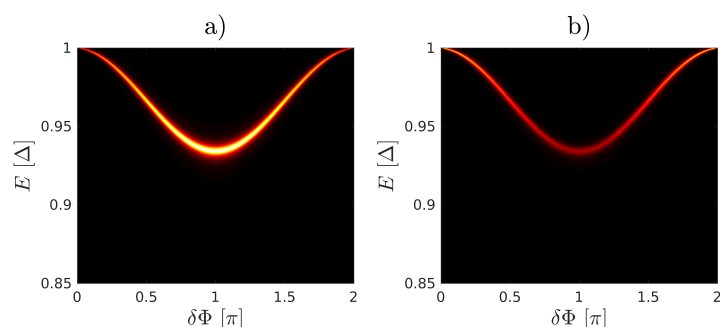


**Figure A3.** The LDOS for electron (a) and hole (b) quasiparticles as a function of  $\delta\Phi$  on molecular site 8 of the Andreev interferometer shown in Figure 6c of the main text and in Figure A1. In these calculations we used  $\varepsilon_3 = -0.50\gamma_0$ .

As mentioned in the “Conclusions and Outlook” section of the main text, by attaching normal leads N1 and N2 to molecular sites 8 and 22 and may enhance the non-local Andreev reflection  $N1 \rightarrow N2$  with respect to the local Andreev reflection  $N1 \rightarrow N1$ .

## References

1. Cuevas, J.C.; Scheer, E. *Molecular Electronics*, 2nd ed.; World Scientific: Singapore, 2017. [[CrossRef](#)]
2. Ratner, M. A brief history of molecular electronics. *Nat. Nanotechnol.* **2013**, *8*, 378–381. [[CrossRef](#)] [[PubMed](#)]
3. Tsutsui, M.; Taniguchi, M. Single Molecule Electronics and Devices. *Sensors* **2012**, *12*, 7259–7298. [[CrossRef](#)] [[PubMed](#)]
4. Lörtscher, E. Wiring molecules into circuits. *Nat. Nanotechnol.* **2013**, *8*, 381–384. [[CrossRef](#)] [[PubMed](#)]
5. Sun, L.; Diaz-Fernandez, Y.A.; Gschneidner, T.A.; Westerlund, F.; Lara-Avila, S.; Moth-Poulsen, K. Single-molecule electronics: from chemical design to functional devices. *Chem. Soc. Rev.* **2014**, *43*, 7378–7411. [[CrossRef](#)] [[PubMed](#)]
6. Su, T.A.; Neupane, M.; Steigerwald, M.L.; Venkataraman, L.; Nuckolls, C. Chemical principles of single-molecule electronics. *Nat. Rev. Mater.* **2016**, *1*, 16002. [[CrossRef](#)]
7. Xiang, D.; Wang, X.; Jia, C.; Lee, T.; Guo, X. Molecular-Scale Electronics: From Concept to Function. *Chem. Rev.* **2016**, *116*, 4318–4440. [[CrossRef](#)]
8. Hybertsen, M.S.; Venkataraman, L. Structure-Property Relationships in Atomic-Scale Junctions: Histograms and Beyond. *Accounts Chem. Res.* **2016**, *49*, 452–460. [[CrossRef](#)]
9. Gehring, P.; Thijssen, J.M.; van der Zant, H.S.J. Single-molecule quantum-transport phenomena in break junctions. *Nat. Rev. Phys.* **2019**, *1*, 381–396. [[CrossRef](#)]
10. Liu, J.; Huang, X.; Wang, F.; Hong, W. Quantum Interference Effects in Charge Transport through Single-Molecule Junctions: Detection, Manipulation, and Application. *Accounts Chem. Res.* **2019**, *52*, 151–160. [[CrossRef](#)]

11. Li, Y.; Yu, X.; Zhen, Y.; Dong, H.; Hu, W. Transmission mechanism and quantum interference in fused thienoacenes coupling to Au electrodes through the thiophene rings. *Phys. Chem. Chem. Phys.* **2019**, *21*, 16293–16301. [[CrossRef](#)]
12. Sangtarash, S.; Huang, C.; Sadeghi, H.; Sorohhov, G.; Hauser, J.; Wandlowski, T.; Hong, W.; Decurtins, S.; Liu, S.X.; Lambert, C.J. Searching the Hearts of Graphene-like Molecules for Simplicity, Sensitivity, and Logic. *J. Am. Chem. Soc.* **2015**, *137*, 11425–11431. [[CrossRef](#)] [[PubMed](#)]
13. Sangtarash, S.; Sadeghi, H.; Lambert, C.J. Exploring quantum interference in heteroatom-substituted graphene-like molecules. *Nanoscale* **2016**, *8*, 13199–13205. [[CrossRef](#)] [[PubMed](#)]
14. Lambert, C.J. Quantum interference from superconducting islands in a mesoscopic solid. *J. Phys. Condens. Matter* **1993**, *5*, 707–716. [[CrossRef](#)]
15. Hui, V.C.; Lambert, C.J. Andreev Scattering, Universal Conductance Fluctuations and Phase Periodic Transport. *Europhys. Lett. (EPL)* **1993**, *23*, 203–209. [[CrossRef](#)]
16. Petrashov, V.T.; Chua, K.G.; Marshall, K.M.; Shaikhaidarov, R.S.; Nicholls, J.T. Andreev Probe of Persistent Current States in Superconducting Quantum Circuits. *Phys. Rev. Lett.* **2005**, *95*, 147001. [[CrossRef](#)]
17. Amado, M.; Fornieri, A.; Biasiol, G.; Sorba, L.; Giazotto, F. A ballistic two-dimensional-electron-gas Andreev interferometer. *Appl. Phys. Lett.* **2014**, *104*, 242604. [[CrossRef](#)]
18. van Wees, B.J.; Lenssen, K.M.H.; Harmans, C.J.P.M. Transmission formalism for supercurrent flow in multiprobe superconductor-semiconductor-superconductor devices. *Phys. Rev. B* **1991**, *44*, 470–473. [[CrossRef](#)]
19. Chang, L.F.; Bagwell, P.F. Control of Andreev-level occupation in a Josephson junction by a normal-metal probe. *Phys. Rev. B* **1997**, *55*, 12678–12690. [[CrossRef](#)]
20. Baselmans, J.J.A.; Morpurgo, A.F.; van Wees, B.J.; Klapwijk, T.M. Reversing the direction of the supercurrent in a controllable Josephson junction. *Nature* **1999**, *397*, 43–45. [[CrossRef](#)]
21. Baselmans, J.J.A.; Heikkilä, T.T.; van Wees, B.J.; Klapwijk, T.M. Direct Observation of the Transition from the Conventional Superconducting State to the  $\pi$  State in a Controllable Josephson Junction. *Phys. Rev. Lett.* **2002**, *89*, 207002. [[CrossRef](#)]
22. Crosser, M.S.; Huang, J.; Pierre, F.; Virtanen, P.; Heikkilä, T.T.; Wilhelm, F.K.; Birge, N.O. Nonequilibrium transport in mesoscopic multi-terminal SNS Josephson junctions. *Phys. Rev. B* **2008**, *77*, 014528. [[CrossRef](#)]
23. Geng, Y.; Sangtarash, S.; Huang, C.; Sadeghi, H.; Fu, Y.; Hong, W.; Wandlowski, T.; Decurtins, S.; Lambert, C.J.; Liu, S.X. Magic Ratios for Connectivity-Driven Electrical Conductance of Graphene-like Molecules. *J. Am. Chem. Soc.* **2015**, *137*, 4469–4476. [[CrossRef](#)] [[PubMed](#)]
24. Winkelmann, C.B.; Roch, N.; Wernsdorfer, W.; Bouchiat, V.; Balestro, F. Superconductivity in a single-C60 transistor. *Nat. Phys.* **2009**, *5*, 876–879. [[CrossRef](#)]
25. Brethau, L.; Girit, Ç.Ö.; Pothier, H.; Esteve, D.; Urbina, C. Exciting Andreev pairs in a superconducting atomic contact. *Nature* **2013**, *499*, 312 [[CrossRef](#)]
26. Weber, D.; Scheer, E. Superconducting properties of lithographic lead break junctions. *Nanotechnology* **2017**, *29*, 045703. [[CrossRef](#)]
27. Island, J.O.; Gaudenzi, R.; de Bruijckere, J.; Burzurí, E.; Franco, C.; Mas-Torrent, M.; Rovira, C.; Veciana, J.; Klapwijk, T.M.; Aguado, R.; et al. Proximity-Induced Shiba States in a Molecular Junction. *Phys. Rev. Lett.* **2017**, *118*, 117001. [[CrossRef](#)]
28. Kormányos, A.; Grace, I.; Lambert, C.J. Andreev reflection through Fano resonances in molecular wires. *Phys. Rev. B* **2009**, *79*, 075119. [[CrossRef](#)]
29. Nappi, C.; Romeo, F.; Parlato, L.; Di Capua, F.; Aloisio, A.; Sarnelli, E. Quantum Interference in Single-Molecule Superconducting Field-Effect Transistors. *J. Phys. Chem. C* **2018**, *122*, 11498–11504. [[CrossRef](#)]
30. Rakyta, P.; Alanazy, A.; Kormányos, A.; Tajkov, Z.; Kukucska, G.; Koltai, J.; Sangtarash, S.; Sadeghi, H.; Cserti, J.; Lambert, C.J. Magic Number Theory of Superconducting Proximity Effects and Wigner Delay Times in Graphene-Like Molecules. *J. Phys. Chem. C* **2019**, *123*, 6812–6822. [[CrossRef](#)]
31. Lambert, C.J. Basic concepts of quantum interference and electron transport in single-molecule electronics. *Chem. Soc. Rev.* **2015**, *44*, 875–888. [[CrossRef](#)]
32. Sadeghi, H.; Mol, J.A.; Lau, C.S.; Briggs, G.A.D.; Warner, J.; Lambert, C.J. Conductance enlargement in picoscale electroburnt graphene nanojunctions. *Proc. Natl. Acad. Sci. USA* **2015**, *112*, 2658–2663. [[CrossRef](#)] [[PubMed](#)]

33. Sedghi, G.; García-Suárez, V.M.; Esdaile, L.J.; Anderson, H.L.; Lambert, C.J.; Martín, S.; Bethell, D.; Higgins, S.J.; Elliott, M.; Bennett, N.; et al. Long-range electron tunnelling in oligo-porphyrin molecular wires. *Nat. Nanotechnol.* **2011**, *6*, 517. [[CrossRef](#)] [[PubMed](#)]
34. Zhao, X.; Huang, C.; Gulcur, M.; Batsanov, A.S.; Baghernejad, M.; Hong, W.; Bryce, M.R.; Wandlowski, T. Oligo(aryleneethynylene)s with Terminal Pyridyl Groups: Synthesis and Length Dependence of the Tunneling-to-Hopping Transition of Single-Molecule Conductances. *Chem. Mater.* **2013**, *25*, 4340–4347. [[CrossRef](#)]
35. Papadopoulos, T.A.; Grace, I.M.; Lambert, C.J. Control of electron transport through Fano resonances in molecular wires. *Phys. Rev. B* **2006**, *74*, 193306. [[CrossRef](#)]
36. Markussen, T.; Schiötz, J.; Thygesen, K.S. Electrochemical control of quantum interference in anthraquinone-based molecular switches. *J. Chem. Phys.* **2010**, *132*, 224104. [[CrossRef](#)]
37. Vazquez, H.; Skouta, R.; Schneebeli, S.; Kamenetska, M.; Breslow, R.; Venkataraman, L.; Hybertsen, M.S. Probing the conductance superposition law in single-molecule circuits with parallel paths. *Nat. Nanotechnol.* **2012**, *7*, 663–667. [[CrossRef](#)]
38. Ballmann, S.; Härtle, R.; Coto, P.B.; Elbing, M.; Mayor, M.; Bryce, M.R.; Thoss, M.; Weber, H.B. Experimental Evidence for Quantum Interference and Vibrationally Induced Decoherence in Single-Molecule Junctions. *Phys. Rev. Lett.* **2012**, *109*, 056801. [[CrossRef](#)]
39. Aradhya, S.V.; Meisner, J.S.; Krikorian, M.; Ahn, S.; Parameswaran, R.; Steigerwald, M.L.; Nuckolls, C.; Venkataraman, L. Dissecting Contact Mechanics from Quantum Interference in Single-Molecule Junctions of Stilbene Derivatives. *Nano Lett.* **2012**, *12*, 1643–1647. [[CrossRef](#)]
40. Arroyo, C.R.; Tarkuc, S.; Frisenda, R.; Seldenthuis, J.S.; Woerde, C.H.M.; Eelkema, R.; Grozema, F.C.; van der Zant, H.S.J. Signatures of Quantum Interference Effects on Charge Transport Through a Single Benzene Ring. *Angew. Chem. Int. Ed.* **2013**, *52*, 3152–3155. [[CrossRef](#)]
41. Guedon, C.M.; Valkenier, H.; Markussen, T.; Thygesen, K.S.; Hummelen, J.C.; van der Molen, S.J. Observation of quantum interference in molecular charge transport. *Nat. Nanotechnol.* **2012**, *7*, 305–309. [[CrossRef](#)]
42. Manrique, D.Z.; Huang, C.; Baghernejad, M.; Zhao, X.; Al-Owaedi, O.A.; Sadeghi, H.; Kaliginedi, V.; Hong, W.; Gulcur, M.; Wandlowski, T.; et al. A quantum circuit rule for interference effects in single-molecule electrical junctions. *Nat. Commun.* **2015**, *6*, 1–8. [[CrossRef](#)] [[PubMed](#)]
43. Famili, M.; Jia, C.; Liu, X.; Wang, P.; Grace, I.M.; Guo, J.; Liu, Y.; Feng, Z.; Wang, Y.; Zhao, Z.; et al. Self-Assembled Molecular-Electronic Films Controlled by Room Temperature Quantum Interference. *Chem* **2019**, *5*, 474–484. [[CrossRef](#)]
44. Della Rocca, M.L.; Chauvin, M.; Huard, B.; Pothier, H.; Esteve, D.; Urbina, C. Measurement of the Current-Phase Relation of Superconducting Atomic Contacts. *Phys. Rev. Lett.* **2007**, *99*, 127005. [[CrossRef](#)] [[PubMed](#)]
45. Nanda, G.; Aguilera-Servin, J.L.; Rakyta, P.; Kormányos, A.; Kleiner, R.; Koelle, D.; Watanabe, K.; Taniguchi, T.; Vandersypen, L.M.K.; Goswami, S. Current-Phase Relation of Ballistic Graphene Josephson Junctions. *Nano Lett.* **2017**, *17*, 3396–3401. [[CrossRef](#)] [[PubMed](#)]
46. Andreev, A.F. The Thermal Conductivity of the Intermediate State in Superconductors. *Zh. Eksp. Teor. Fiz.* **1964**, *46*, 1823–1828.
47. Bagwell, P.F. Suppression of the Josephson current through a narrow, mesoscopic, semiconductor channel by a single impurity. *Phys. Rev. B* **1992**, *46*, 12573–12586. [[CrossRef](#)] [[PubMed](#)]
48. Cresti, A.; Farchioni, R.; Grosso, G.; Parravicini, G.P. Keldysh-Green function formalism for current profiles in mesoscopic systems. *Phys. Rev. B* **2003**, *68*, 075306. [[CrossRef](#)]
49. Do, V.N. Non-equilibrium Green function method: Theory and application in simulation of nanometer electronic devices. *Adv. Nat. Sci. Nanosci. Nanotechnol.* **2014**, *5*, 033001. [[CrossRef](#)]
50. Pala, M.G.; Governale, M.; König, J. Nonequilibrium Josephson and Andreev current through interacting quantum dots. *New J. Phys.* **2007**, *9*, 278–278. [[CrossRef](#)]
51. Eötvös Quantum Utilities Software Package. Available online: <http://eqt.elte.hu/EQuUs/html/> (accessed on 2 May 2020).
52. Claughton, N.R.; Leadbeater, M.; Lambert, C.J. Theory of Andreev resonances in quantum dots. *J. Phys. Condens. Matter* **1995**, *7*, 8757–8784. [[CrossRef](#)]
53. Russo, S.; Kroug, M.; Klapwijk, T.M.; Morpurgo, A.F. Experimental Observation of Bias-Dependent Nonlocal Andreev Reflection. *Phys. Rev. Lett.* **2005**, *95*, 027002. [[CrossRef](#)] [[PubMed](#)]

54. Hofstetter, L.; Csonka, S.; Nygård, J.; Schönenberger, C. Cooper pair splitter realized in a two-quantum-dot Y-junction. *Nature* **2009**, *461*, 960–963. [[CrossRef](#)] [[PubMed](#)]
55. Herrmann, L.G.; Portier, F.; Roche, P.; Yeyati, A.L.; Kontos, T.; Strunk, C. Carbon Nanotubes as Cooper-Pair Beam Splitters. *Phys. Rev. Lett.* **2010**, *104*, 026801. [[CrossRef](#)] [[PubMed](#)]
56. Hofstetter, L.; Csonka, S.; Baumgartner, A.; Fülöp, G.; d’Hollosy, S.; Nygård, J.; Schönenberger, C. Finite-Bias Cooper Pair Splitting. *Phys. Rev. Lett.* **2011**, *107*, 136801. [[CrossRef](#)]
57. Cayssol, J. Crossed Andreev Reflection in a Graphene Bipolar Transistor. *Phys. Rev. Lett.* **2008**, *100*, 147001. [[CrossRef](#)]
58. Chen, W.; Shen, R.; Sheng, L.; Wang, B.G.; Xing, D.Y. Resonant nonlocal Andreev reflection in a narrow quantum spin Hall system. *Phys. Rev. B* **2011**, *84*, 115420. [[CrossRef](#)]
59. Schroer, A.; Silvestrov, P.G.; Recher, P. Valley-based Cooper pair splitting via topologically confined channels in bilayer graphene. *Phys. Rev. B* **2015**, *92*, 241404. [[CrossRef](#)]
60. Bolech, C.J.; Giamarchi, T. Keldysh study of point-contact tunneling between superconductors. *Phys. Rev. B* **2005**, *71*, 024517. [[CrossRef](#)]
61. Wu, S.T.; Yip, S. ac Josephson effect in asymmetric superconducting quantum point contacts. *Phys. Rev. B* **2004**, *70*, 104511. [[CrossRef](#)]
62. Rungger, I.; Sanvito, S. Algorithm for the construction of self-energies for electronic transport calculations based on singularity elimination and singular value decomposition. *Phys. Rev. B* **2008**, *78*, 035407. [[CrossRef](#)]



© 2020 by the authors. Licensee MDPI, Basel, Switzerland. This article is an open access article distributed under the terms and conditions of the Creative Commons Attribution (CC BY) license (<http://creativecommons.org/licenses/by/4.0/>).